https://doi.org/10.5194/ms-2026-192
Preprint. Discussion started: 3 November 2026
© Author(s) 2026. CC BY 4.0 License.



mechanical sciences
DISCUSSIONS

A Coupled Crystal Plasticity-Phase-Field Damage Model for Integrated CAD/CAE-Based Fatigue Design of Rolling Bearings

Chao Ji[1], Weiqi Du[1,*], Yandong Zhao[2], Yibin Wu[1]

[1]School of Mechanical Engineering and Intelligent Manufacturing, Ningbo University, Ningbo 315211, China

[2]Ningbo Delikebei Technology Co., Ltd, Ningbo 315600, China

[*]Correspondence: Weiqi Du (duweiqi@nbu.edu.cn)

Abstract

This study proposes an integrated multiscale method for rolling contact fatigue (RCF) life prediction of rolling bearings. A dimension-chain mapping drives parametric reconstruction and macroscale contact analysis. The contact parameters are transferred to a grain-scale crystal plasticity-phase-field model as a moving Hertzian load. A three-layer solution framework with a cycle-jump scheme calculates damage evolution. Results show that an elliptical Al_2O_3 inclusion promotes crack initiation and significantly reduces the predicted life. A larger rolling-element diameter extends the life, while a larger raceway curvature coefficient or positive radial clearance shortens the life.

Keywords: rolling contact fatigue; crystal plasticity; phase-field method; multiscale analysis

Nomenclature

α	Contact half-width	$\dot{\gamma}^{\alpha}$	Shear rate on slip system
b_j	Fatigue life exponent	$\dot{\gamma}^{0}$	Reference shear rate
D	Fatigue accumulation variable	η_h	Fraction of slip work converted to stored energy
D_T	Fatigue accumulation threshold	μ	Friction coefficient
G_c	Fracture toughness	τ^{α}	Resolved shear stress on slip system
H	History field	τ_c^{α}	Critical resolved shear stress on slip system
J	Cycle-jump factor	$\tau_{c,0}$	Initial critical resolved shear stress
ℓ	Phase-field length scale	$\tau_{c,s}$	Saturation critical resolved shear stress
m	Rate-sensitivity exponent	$\tau_{MOSS,j}$	Maximum orthogonal shear stress (MOSS) for raceway
n	Rotational speed	$\tau_{ref,j}$	Reference MOSS for raceway
N_{eq}	Equivalent number of cycles	ϕ	Phase-field variable
$N_{f,b}$	Bearing fatigue life from competing-failure relation	ψ_e^{+}	Tensile elastic strain energy
$N_{f,j}$	Predicted RCF life of raceway	ψ_e^{-}	Compressive elastic strain energy
N_{ref}	Reference RCF life from grain-scale model	$\psi_{p,hard}$	Accumulated stored plastic work
N_s	Number of slip systems	p_0	Peak contact pressure

1. Introduction

Rolling bearings are key machine elements for load transfer and motion constraint in

https://doi.org/10.5194/ms-2026-192
Preprint. Discussion started: 3 November 2026
© Author(s) 2026. CC BY 4.0 License.



mechanical sciences
DISCUSSIONS

rotating machinery. Raceway pitting and spalling cause vibration, noise, and loss of accuracy. Severe damage can lead to system failure. When rolling elements repeatedly pass through the loaded zone, the raceways experience high-amplitude cyclic contact stresses with steep spatial gradients that move along the raceway. Plastic slip and microstructural damage then accumulate near or below the surface. Cracks form and grow toward the free surface. This process is controlled by the load and contact geometry. It is also sensitive to radial clearance, raceway curvature, rolling-element size, rotational speed, grain orientation, and nonmetallic inclusions. Rolling contact fatigue (RCF) in rolling bearings therefore involves a multiscale link among structural parameters, the macroscale contact field, grain-scale plastic localization, and crack evolution.

For engineering life assessment, the Lundberg–Palmgren theory established the basic rating-life model based on contact stress, stressed volume, and Weibull statistics (Lundberg and Palmgren, 1947; Harris and Kotzalas, 2006). Ioannides and Harris later introduced a fatigue-limit stress and modified the contribution of low-stress regions to fatigue damage (Ioannides and Harris, 1985). The Jones–Harris method, five-degree-of-freedom quasi-static models, and their extensions calculate rolling-element load distribution, contact angle, centrifugal force, and speed-dependent stiffness (Jones, 1959; de Mul et al., 1989; Kang et al., 2006; Fang et al., 2019). These models support efficient assessments of structural and operating parameters. Recent work has also examined the effects of rolling-element position and parameter uncertainty on bearing fatigue life (Cheng and Zhang, 2022). Such methods are suitable for engineering selection and parameter scans. However, they usually describe failure using macroscale contact stress or empirical life variables. They cannot fully explain life differences caused by grain orientation, local slip, or inclusion geometry under the same nominal load. They also do not directly predict crack initiation sites and spalling evolution.

Crystal plasticity finite element models describe the anisotropic deformation of polycrystals through slip-system kinetics and hardening laws. They can resolve the localization of resolved shear stress, plastic slip, and dissipated work under cyclic loading (Hill and Rice, 1972; Huang, 1991; McDowell and Dunne, 2010; Wan et al., 2014). Zhang et al. developed a dislocation-density-based crystal plasticity damage model for the RCF of gradient-grained structures (Zhang et al., 2024). Xiong et al. studied the effect of nonmetallic inclusions on RCF damage (Xiong et al., 2024). Vijay and Sadeghi combined crystal plasticity with cohesive elements to simulate crack initiation, propagation, and final spalling in bearing steels (Vijay and Sadeghi, 2022). Han et al. further investigated micropit formation and its dependence on the microstructure (Han et al., 2024). These studies show that local plasticity

https://doi.org/10.5194/ms-2026-192
Preprint. Discussion started: 3 November 2026
© Author(s) 2026. CC BY 4.0 License.



mechanical sciences
DISCUSSIONS

within grains and near grain boundaries plays an important role in RCF crack initiation. However, cohesive elements usually require predefined potential crack paths. Models based on fatigue indicator parameters also have difficulty describing the continuous competition, deflection, and coalescence of multiple cracks.

Phase-field fracture uses a continuous variable to describe material integrity. It regularizes a discrete crack surface as a finite-width damage band. Crack initiation, growth, branching, and coalescence can therefore be modeled without explicit crack tracking (Francfort and Marigo, 1998; Miehe et al., 2010; Ambati et al., 2015; Golahmar et al., 2023). Polančec et al. applied a plasticity–fatigue phase-field model to rolling-contact pitting and reproduced both surface- and subsurface-initiated spalling patterns (Polančec et al., 2023). Lucarini et al. proposed a stored-energy-based crystal plasticity phase-field model and studied fatigue cracking at the grain scale (Lucarini et al., 2023). Zhang et al. recently developed a plasticity–fatigue phase-field model for rolling-contact spalling (Zhang et al., 2025). These advances show that crystal plasticity and the phase-field method can jointly describe slip localization and complex crack evolution. However, the computational cost remains high. In addition, most local models are driven by prescribed Hertzian loads and are not automatically linked to bearing structural parameters or macroscale contact fields.

Computer-aided design and computer-aided engineering (CAD/CAE) integration has developed from file exchange to parameter association, shared data models, and multi-domain feature mapping. Khan and Rezwana reviewed geometric simplification, data formats, and semantic preservation in CAD-to-CAE conversion (Khan and Rezwana, 2021). Li et al. linked design, finite element, and evaluation models through multi-domain feature mapping (Li et al., 2023). Existing integration methods mainly address conversion and consistency between geometric and finite element models. In bearing RCF research, structural contact analysis and local damage simulation are still often performed separately. A key task is to transfer the effect of structural parameters on the macroscale contact field to a microstructure-sensitive damage model. The predicted life must then be returned to the structural-parameter assessment. This connection is needed to integrate bearing modeling, simulation, life assessment, and parameter feedback.

This study develops an integrated multiscale platform for rolling bearings. Python coordinates SolidWorks and Abaqus. A hierarchical dimension chain maintains consistent relations among structural parameters, CAD features, assembly constraints, and CAE objects. The platform automatically reconstructs the bearing, performs macroscale contact analysis, and extracts key contact parameters. The macroscale results are then converted into a moving

https://doi.org/10.5194/ms-2026-192
Preprint. Discussion started: 3 November 2026
© Author(s) 2026. CC BY 4.0 License.



mechanical sciences
DISCUSSIONS

Hertzian load on a local polycrystalline model. A direct combination of a crystal plasticity UMAT, a phase-field UEL, and a residual-control UEL does not provide the required data exchange. Therefore, this work reorganizes the transfer and solution sequence of stored plastic work, the phase-field degradation variable, and staggered-iteration residuals. This forms a three-layer crystal plasticity-phase-field solution method for moving contact loads.

The remainder of this paper is organized as follows: Section 2 describes the integrated multiscale analysis platform. Section 3 presents the coupled crystal plasticity-phase-field model. Section 4 provides the results and discussion. Section 5 summarizes the main conclusions.

2. Integrated multiscale analysis platform

2.1 Overall architecture and task loop

The platform contains four functional layers: interaction and scheduling, analysis and computation, data and criteria, and parameter feedback. The workflow has five stages: parameter definition, parametric modeling, macroscale contact analysis, multiscale analysis, and life assessment. The interaction and scheduling layer receives structural, material, and operating parameters. It also coordinates SolidWorks and Abaqus. The analysis layer performs parametric modeling, macroscale contact analysis, and crystal plasticity–phase-field life calculation. The data layer stores dimension chains, contact results, and life criteria. The feedback layer generates or screens the next parameter sets using predicted life and geometric constraints. These parameters are then returned to the modeling and analysis workflow.

Each analysis task is linked to a parameter file, a CAD model, a macroscale finite element job, a multiscale load file, and a life result. Python first checks the parameter ranges and dimensional constraints. It then calls SolidWorks to rebuild the parts and assembly. After the geometry passes the checks, an Abaqus script creates and submits the macroscale contact model. Post-processing converts the macroscale results into loads for the grain-scale model. The predicted life is finally returned to the parameter-update module.

The platform executes parameter checking, CAD reconstruction, macroscale solution, result extraction, multiscale mapping, life assessment, and parameter updating in sequence. A stage starts only after the previous stage has finished and passed its checks. If a task is interrupted, the platform retains the current parameters and available results. The job can then restart from the interrupted stage. This process prevents invalid geometry or unconverged results from entering later modules.

The modules exchange data through structured files. A parameter file records field names,

https://doi.org/10.5194/ms-2026-192
Preprint. Discussion started: 3 November 2026
© Author(s) 2026. CC BY 4.0 License.



mechanical sciences DISCUSSIONS

values, and units. A macroscale result file stores contact pressure, contact size, and maximum orthogonal shear stress for the inner and outer raceways. A grain-scale load file stores the moving load and cycle-control parameters. A common task identifier links all files. This maintains consistency among the CAD model, finite element results, and life output.

2.2 Dimension-chain mapping and parametric modeling module

The parametric modeling module uses overall dimensions, rolling-element parameters, raceway parameters, and assembly parameters as common inputs. The independent input vector is $x_{CAD} = \{D, d, B, D_w, Z, f, G_r\}$. Table. 1 shows the intermediate dimensions generated by the dimension chain. The constraint chain updates the inner ring, outer ring, rolling elements, cage, and assembly at the same time.

Python reads the dimension chain and writes it to the SolidWorks template. It then rebuilds the parts, updates the assembly, and checks for interference. One set of master parameters drives the inner ring, outer ring, rolling elements, and cage. The mapping relations calculate all derived dimensions automatically. This avoids assembly inconsistency caused by separate modifications of individual parts. After the checks, the model is saved and the CAD functional tags are transferred to the finite element module.

(a) Bearing Parameter Symbol Cross -Reference Table

Symbol	Parameter Name
D	Bearing Outside Diameter
d	Bearing Bore Diameter
B	Bearing Width
C_1	Outer Ring Thickness
C_2	Inner Ring Thickness
r	Raceway Radius
D_W	Ball Diameter
a	Ball Contact Angle
Z	Number of Rolling Elements

(b) Dimensional Chain Mapping Table

Constraints	Input Parameters	Output Components and Dimensions	Correspondence
Bearing Outside Diameter	D	Outer Ring Outside Diameter	D
Bearing Bore Diameter	d	Inner Ring Bore Diameter	d
Bearing Width	B	Overall Bearing Width	B
Outer Ring Thickness	C_1	Outer Ring Radial Thickness	C_1
Inner Ring Thickness	C_2	Inner Ring Radial Thickness	C_2
Raceway Radius	r	Raceway Curvature Radius of Inner and Outer Rings	r
Ball Diameter	D_W	Rolling Element Diameter	D_W
Ball Contact Angle	a	Rolling Element Contact Angle	a
Number of Rolling Elements	Z	Rolling Element Count	Z
Cage Inner Diameter	–	Cage Inner Diameter	Cage Inner Diameter
Cage Outer Diameter	–	Cage Outer Diameter	Cage Outer Diameter
Number of Inner Cage Pockets	–	Number of Cage Pockets	Number of Inner Cage Pockets
Number of Outer Cage Pockets	–	Number of Cage Pockets	Number of Outer Cage Pockets
Outer Ring Raceway Pitch Diameter	D, C_1	Outer Ring Raceway Center Diameter	$D_1 = D - C_1$
Inner Ring Raceway Pitch Diameter	d, C_2	Inner Ring Raceway Center Diameter	$D_1 = d + C_2$
Radial Internal Clearance	D, d, D_W, C_1, C_2	Bearing Radial Clearance	$G_r = D - d - 2C_1 - 2C_2 - D_W$
Mounting Height	D_W, a	Bearing Assembly Height	$H = D_W \times [1 - \cos(\alpha)]/2$

Table 1. Dimension-chain mapping and transfer of structural parameters.

Fig. 1 shows the interface of this module.Functional-object mapping is used between CAD and CAE. The Abaqus script identifies contact, loading, and constrained surfaces from functional tags, spatial positions, and surface normals. These analysis objects can therefore be

https://doi.org/10.5194/ms-2026-192
Preprint. Discussion started: 3 November 2026
© Author(s) 2026. CC BY 4.0 License.



mechanical sciences DISCUSSIONS

rebuilt after structural parameters change. Manual reselection after each geometric update is not needed.

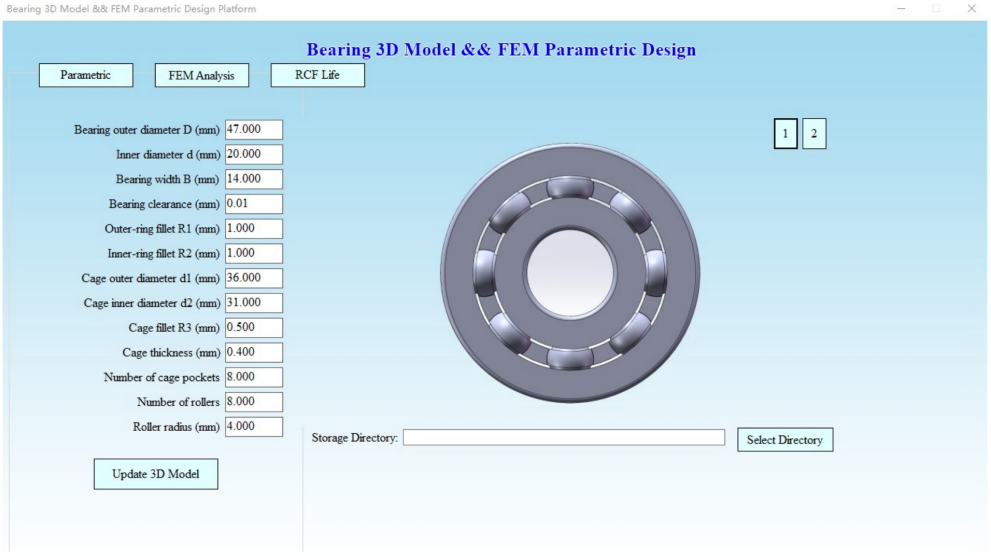


Fig. 1. Interface of the parametric modeling module.

2.3 Automated macroscale contact analysis module

Fig. 2 shows the interface of the macroscale finite element analysis module. The finite element module receives the parametric assembly model and the operating-condition file. Abaqus scripts then import the geometry, assign materials, define contact, apply boundary conditions, generate the mesh, and submit the job. A locally refined mesh is used in the rolling-element–raceway contact zones. The mesh size gradually increases outside these zones. After the user submits a task, model construction, solution monitoring, and result extraction run in sequence. Before submission, the module checks the geometry import, contact-pair integrity, initial overclosure, and mesh quality. After completion, it checks convergence and the integrity of the result file.

https://doi.org/10.5194/ms-2026-192
Preprint. Discussion started: 3 November 2026
© Author(s) 2026. CC BY 4.0 License.



mechanical sciences DISCUSSIONS

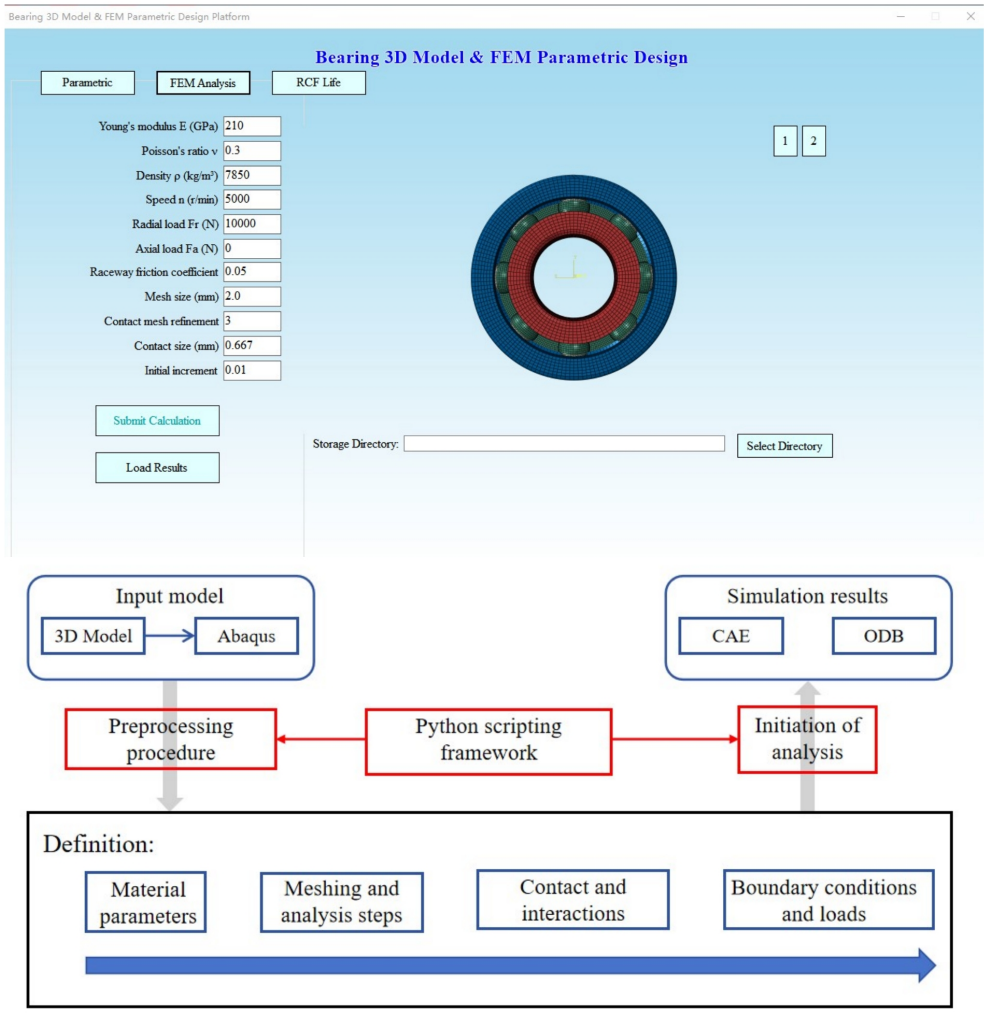


Fig. 2. Interface and workflow of the macroscale finite element analysis module.

Fig. 3 shows the automatic construction and execution of the macroscale finite element model.The post-processing program reads the contact pressure and subsurface stress of the inner and outer raceways. It automatically extracts the peak contact pressure p_0, the contact half-width a in the rolling direction, and the maximum orthogonal shear stress (MOSS), τ_{MOSS}. The values of p_0 and a define the grain-scale moving load. The value of τ_{MOSS} is used to compare fatigue severity and calculate life for different structural parameters. Rotational speed enters the macroscale contact calculation as an operating parameter. The resulting contact field is then transferred to the life module. Standardized load data are exported for direct use by the grain-scale model and life calculation.

https://doi.org/10.5194/ms-2026-192
Preprint. Discussion started: 3 November 2026
© Author(s) 2026. CC BY 4.0 License.



mechanical sciences
DISCUSSIONS

The macroscale ball–raceway contact patch is elliptical, whereas the grain-scale model uses a two-dimensional plane-strain geometry. The platform extracts the main contact section through the pressure peak along the rolling direction. It converts this section into a two-dimensional moving Hertzian load with the same p_0 and half-width a. Model construction, job monitoring, and result extraction are controlled from the interface.

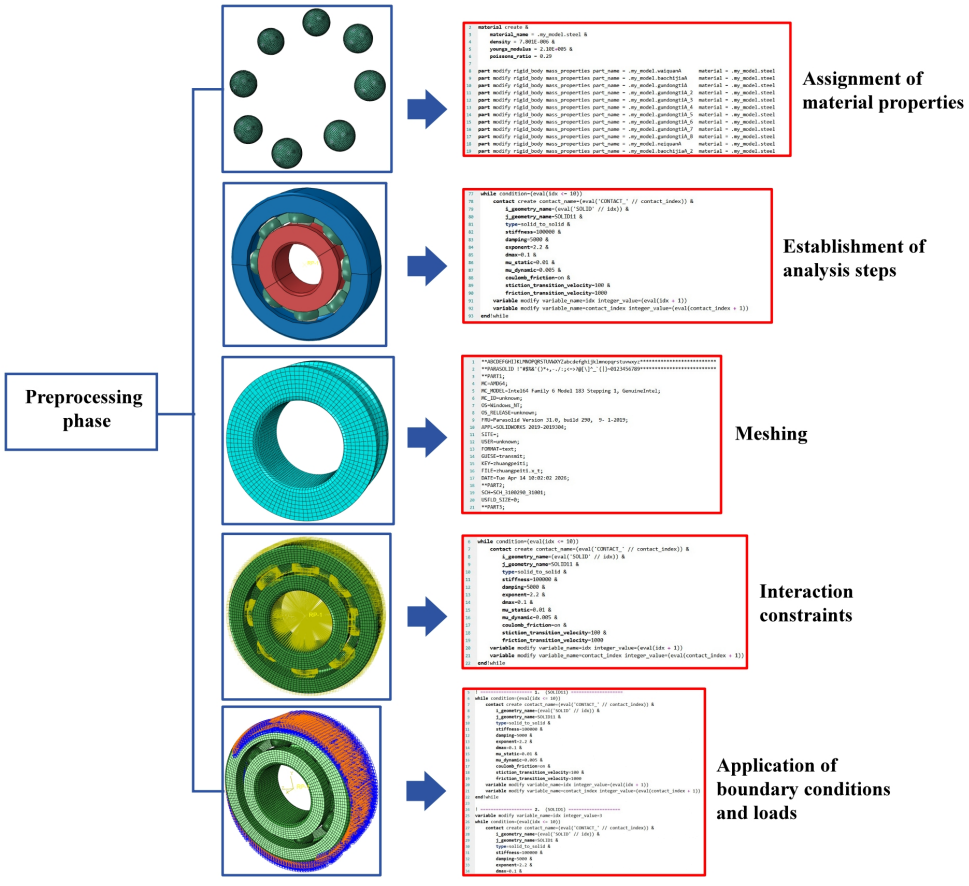


Fig. 3. Automatic construction and execution of the macroscale finite element model.

2.4 Automated grain-scale model construction and life prediction module

Fig. 4 shows the interface of the grain-scale modeling and life prediction module. This module integrates local polycrystalline model generation, material-parameter assignment, multiscale load transfer, job submission, and life assessment. The user can specify the model size, number of grains, and mean grain size in the interface. The program then generates the polycrystalline geometry, creates the mesh, and builds material and element sets from the grain identifiers. Elastic parameters, crystal plasticity parameters, and crystal orientations are

https://doi.org/10.5194/ms-2026-192
Preprint. Discussion started: 3 November 2026
© Author(s) 2026. CC BY 4.0 License.



mechanical sciences DISCUSSIONS

written in batches from a parameter file. No grain needs to be defined manually.

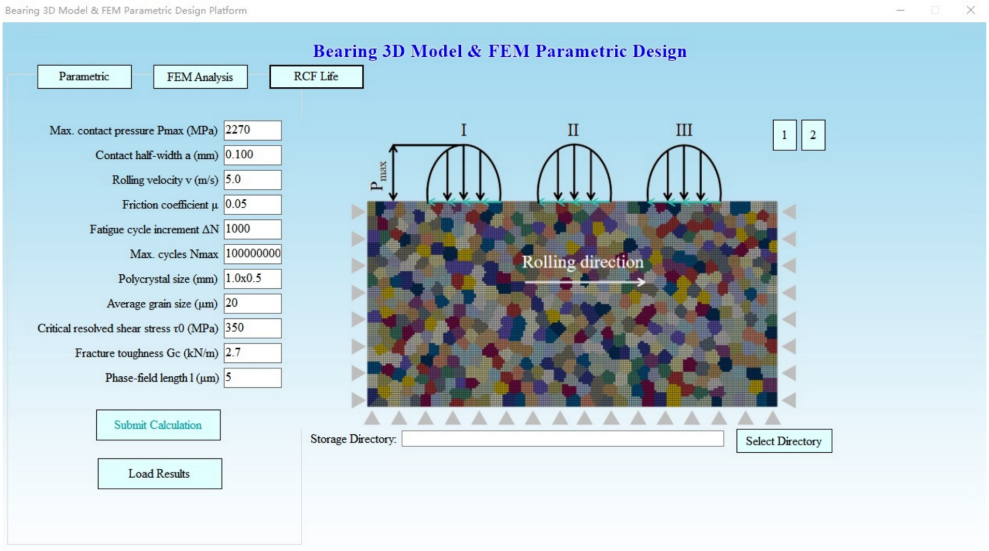


Fig. 4. Interface of the grain-scale modeling and life prediction module.

After model construction, the module reads the peak contact pressure p_0 and contact half-width a from the macroscale analysis. It also reads the friction coefficient, rolling direction, and cycle-control parameters. The program automatically defines the moving contact load, boundary conditions, and crystal plasticity–phase-field analysis steps. After the user selects “Submit Calculation,” it generates the input file, links the user subroutines, creates the job, and starts the analysis. Fig. 5 shows the automatic construction of the grain-scale model and assignment of material parameters. When the calculation ends, it extracts the phase-field variable and evaluates the life criterion. Thus, the same interface covers the full process from grain-scale parameter input to simulation. Section 4.1 gives the material parameters, moving-load function, cycle-jump setting, and life criterion.

https://doi.org/10.5194/ms-2026-192
Preprint. Discussion started: 3 November 2026
© Author(s) 2026. CC BY 4.0 License.



mechanical sciences
DISCUSSIONS

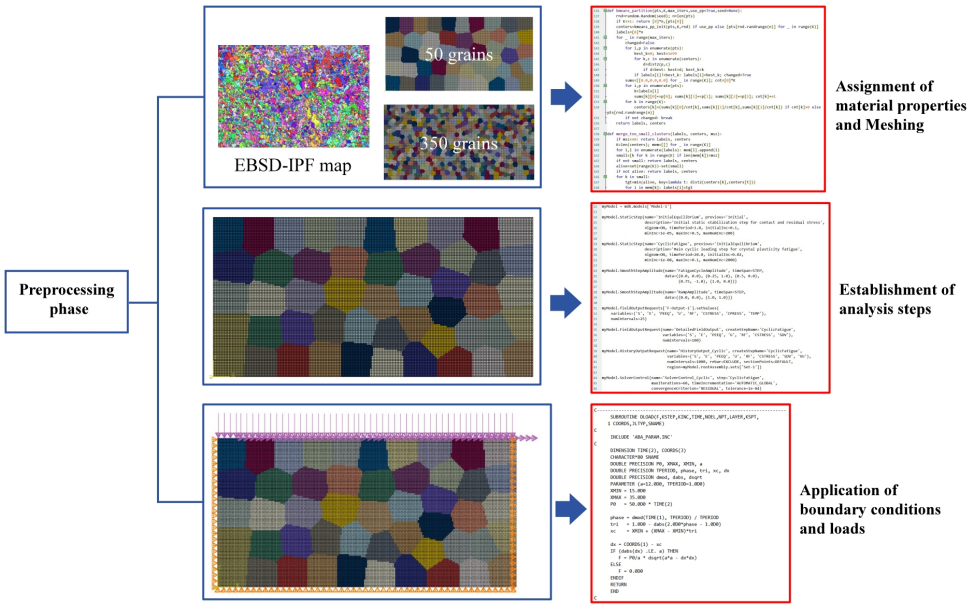


Fig. 5. Automatic construction of the grain-scale model and assignment of material parameters.

A complete crystal plasticity–phase-field simulation for every candidate design would be computationally expensive. The platform therefore uses the phase-field life of a reference condition as the baseline. The MOSS obtained from the macroscale model is then used to convert each parameter set into predicted inner- and outer-raceway lives:

$$N_{f,j} = N_{ref}\left(\frac{\tau_{ref,j}}{\tau_{MOSS,j}}\right)^{b_j}, j = i,o \tag{1}$$

where j = i and j = o refer to the inner and outer raceways, respectively. N_{ref} is the equivalent RCF damage life from the grain-scale phase-field model under the reference condition. $\tau_{\mathrm{ref},j}$ is the MOSS of the corresponding raceway from the macroscale model under the same condition. $\tau_{\mathrm{MOSS},j}$ is the MOSS for the current parameter set. Following the inner- and outer-raceway MOSS–life relation used in Cheng and Zhang (2022), b_i = 3.05 and b_o = 2.90 are adopted. Both exponents remain constant in all parameter scans. Equation (1) uses one grain-scale reference life to convert the macroscale MOSS of each parameter set into predicted lives for both raceways. The bearing life is then obtained from the competing-failure relation:

$$N_{f,b} = \left[N_{f,i}^{-10/9} + N_{f,o}^{-10/9}\right]^{-9/10} \tag{2}$$

Equation (2) combines the inner- and outer-raceway lives using the independent competing-failure relation (Lundberg and Palmgren, 1947; Ioannides and Harris, 1985; Harris and Kotzalas, 2006).

https://doi.org/10.5194/ms-2026-192
Preprint. Discussion started: 3 November 2026
© Author(s) 2026. CC BY 4.0 License.



mechanical sciences
DISCUSSIONS

After the life result returns to the parameter-update module, the platform performs predefined scans of rolling-element diameter, raceway curvature coefficient, and radial clearance. At each speed, the platform completes dimension checking, model reconstruction, macroscale analysis, and life calculation for each parameter set.

After each scan, the platform compares the overall bearing lives and reports the life response and screened parameters. The module can run a complete crystal plasticity–phase-field simulation for one condition. It can also use the reference result for batch life assessment of structural parameters.

3. Coupled crystal plasticity–phase-field model

3.1 Rate-dependent crystal plasticity constitutive model

A rate-dependent crystal plasticity model is used to describe the accumulation of inelastic deformation in bearing steel under repeated rolling contact (Hill and Rice, 1972; Huang, 1991). The grain-scale domain is discretized under a two-dimensional plane-strain constraint. It satisfies $\varepsilon_{33} = \gamma_{13} = \gamma_{23} = 0$ and retains the out-of-plane stress σ_{33}. The material response at each integration point is updated by a modified version of Huang's crystal plasticity UMAT through shear on the slip systems. Each material point considers the 12 {110}〈111〉 slip systems of a body-centered cubic (BCC) crystal, so $N_s = 12$. The slip directions and slip-plane normals of each grain are rotated according to its crystal orientation. According to Schmid's law, the plastic strain-rate tensor is

$$\dot{\varepsilon}_p = \sum_{\alpha=1}^{N_s} \dot{\gamma}^{\alpha} P^{\alpha} \tag{3}$$

where N_S is the number of slip systems, $\dot{\gamma}^{\alpha}$ is the shear rate on slip system α, and P^{α} is the corresponding symmetric Schmid tensor. The slip direction s^{α} and slip-plane normal m^{α} are determined by the crystal orientation as follows:

$$P^{\alpha} = \frac{1}{2}\left(m^{\alpha} \otimes s^{\alpha} + s^{\alpha} \otimes m^{\alpha}\right) \tag{4}$$

A rate-dependent power-law equation describes slip under repeated rolling contact. The shear rate α on slip system $\dot{\gamma}^{\alpha}$ is a power-law function of the ratio between the resolved shear stress τ^{α} and the critical resolved shear stress τ_c^{α}:

$$\dot{\gamma}^{\alpha} = \dot{\gamma}^{0} \left| \frac{\tau^{\alpha}}{\tau_c^{\alpha}} \right|^{\frac{1}{m}} \operatorname{sgn}\left(\tau^{\alpha}\right) \tag{5}$$

https://doi.org/10.5194/ms-2026-192
Preprint. Discussion started: 3 November 2026
© Author(s) 2026. CC BY 4.0 License.



mechanical sciences DISCUSSIONS

where $\dot{\gamma}^0$ is the reference shear rate. The quantities τ^α and τ_c^α are the resolved shear stress and critical resolved shear stress on slip system α, respectively. The parameter m is the rate-sensitivity exponent. The model approaches rate-independent crystal plasticity as m approaches zero. The sign function $\mathrm{sgn}\left(\tau^\alpha\right)$ is defined as

$$\mathrm{sgn}\left(\tau^\alpha\right)=\begin{cases}1\ ,\tau^\alpha>0\\0\ ,\tau^\alpha=0\\-1,\tau^\alpha<0\end{cases} \tag{6}$$

The critical resolved shear stress evolves as cyclic plastic deformation accumulates. A saturation hardening law describes self-hardening and latent hardening among the slip systems:

$$\tau_c^\alpha=\tau_{\mathrm{c},0}+\int_0^t\sum_{\beta=1}^{N_s}h_{\alpha\beta}\left|\dot{\gamma}^\beta\right|dt \tag{7}$$

Self-hardening and latent hardening are described by the hardening matrix: $h_{\alpha\beta}$

$$h_{\alpha\beta}=h_0\,\mathrm{sech}^2\left(\frac{h_0\Gamma}{\tau_{c,s}-\tau_{c,0}}\right)q_{\alpha\beta} \tag{8}$$

where $\tau_{c,0}$ and $\tau_{c,s}$ are the initial and saturation critical resolved shear stresses, respectively. The parameter h_0 is the initial hardening modulus, $q_{\alpha\beta}$ is the latent hardening coefficient, and Γ is the accumulated shear over all slip systems. This relation describes self-hardening and latent hardening during cyclic loading.

$$\Gamma=\int_0^t\sum_{\beta=1}^{N_s}\left|\dot{\gamma}^\beta\right|dt \tag{9}$$

The crystal plasticity constitutive model is implemented in an Abaqus UMAT. The undegraded effective stress at an integration point is calculated from the elastic strain and elastic stiffness tensor: $\widetilde{\sigma}$

$$\widetilde{\sigma}=C:\left(\varepsilon-\varepsilon_p\right) \tag{10}$$

3.2 Phase-field damage model driven by accumulated stored plastic work

A variational phase-field method is used to describe crack initiation, propagation, and spalling during RCF (Francfort and Marigo, 1998; Miehe et al., 2010; Ambati et al., 2015; Golahmar et al., 2023). The phase-field variable $\phi\in[0,1]$ describes the material state continuously. The state $\phi=0$ denotes intact material, and $\phi=1$ denotes complete fracture.

https://doi.org/10.5194/ms-2026-192
Preprint. Discussion started: 3 November 2026
© Author(s) 2026. CC BY 4.0 License.



mechanical sciences DISCUSSIONS

The crack-surface density function is

$$\gamma(\phi,\nabla\phi)=\frac{1}{2\ell}\left(\phi^2+l^2|\nabla\phi|^2\right) \tag{11}$$

where ℓ is the phase-field length scale and controls the width of the diffuse crack. In the thermodynamic framework, the crack-driving potential includes degraded tensile elastic strain energy, undegraded compressive elastic strain energy, accumulated stored plastic work, and crack-surface energy:

$$\Psi(\varepsilon,\phi,D)=\int_\Omega\left[g(\phi)\left(\psi_e^+ +\psi_{p,hard}\right)+\psi_e^-\right]d\Omega+\int_\Omega F(D)G_c\gamma(\phi,\nabla\phi)d\Omega \tag{12}$$

where $g(\phi)$ is a quadratic degradation function. It describes the loss of load-carrying stiffness as phase-field damage increases:

$$g(\phi)=(1-\kappa)(1-\phi)^2+\kappa \tag{13}$$

The parameter $\kappa = 10^{-7}$ is the residual-stiffness coefficient. It prevents a singular stiffness matrix in fully damaged regions.

A spectral decomposition of the elastic strain tensor is used to suppress nonphysical crack growth under compression. The elastic strain energy is divided into tensile and compressive parts. The degradation function acts only on the tensile part. Let ψ_e^+ and ψ_e^- denote the positive and negative Macaulay brackets, respectively:

$$\psi_e^{'}=g(\phi)\psi_e^+ +\psi_e^- \tag{14}$$

$$\varepsilon_e=\sum_{i=1}^{3}\varepsilon_i n_i\otimes n_i;\varepsilon_e^{\pm}=\sum_{i=1}^{3}\langle\varepsilon_i\rangle^{\pm}n_i\otimes n_i \tag{15}$$

$$\langle x\rangle^{\pm}=\frac{x\pm|x|}{2};\psi_e^{\pm}=\frac{1}{2}\varepsilon_e^{\pm}:C:\varepsilon_e^{\pm} \tag{16}$$

The corresponding undegraded tensile and compressive stresses are $\widetilde{\sigma}^{\pm}=C:\varepsilon_e^{\pm}$.

Most plastic work in bearing steel is dissipated as heat during cyclic deformation. Part of this work is stored in dislocation structures and microstructural defects and contributes to fatigue crack initiation (Wan et al., 2014; Lucarini et al., 2023). The accumulated stored plastic work represents this stored component and provides an additional driving force for phase-field evolution:

$$\psi_{p,hard}=\int_0^t\eta_h\sum_{\alpha=1}^{N_s}\tau^\alpha\dot{\gamma}^\alpha dt \tag{17}$$

where η_h is the fraction of slip work converted into stored hardening energy. According to

https://doi.org/10.5194/ms-2026-192
Preprint. Discussion started: 3 November 2026
© Author(s) 2026. CC BY 4.0 License.



mechanical sciences DISCUSSIONS

Eq. (5), τ^{α} and $\dot{\gamma}^{\alpha}$ have the same sign. The UMAT updates the accumulated stored plastic work at each integration point and transfers it to the phase-field UEL. The history field H stores the maximum tensile elastic strain energy reached during loading and enforces irreversible damage evolution.

$$H_n^k = \max\left\{H_n^{k-1}, \psi_e^+\left[\varepsilon_e\left(u_n^h\right)\right]\right\} \tag{18}$$

3.3 Fatigue degradation model based on cyclic accumulation

A single load pass is usually insufficient to cause monotonic fracture under RCF conditions. Repeated rolling contact instead produces continuous local damage accumulation. A cyclic history variable and a fatigue degradation function are introduced into the phase-field equation to describe this subcritical degradation (Golahmar et al., 2023). The function reduces the effective fracture resistance. Cracks can therefore grow under cyclic loads below the monotonic fracture threshold:

$$F(D) = \begin{cases} 1 & , D \le D_T \\ \left(\dfrac{2D_T}{D + D_T}\right)^2 & , D > D_T \end{cases} \tag{19}$$

where D_T is the fatigue accumulation threshold. According to the energy-threshold definition of the AT2 fatigue phase-field model (Golahmar et al., 2023), $D_T = G_c/(12\ell) = 45$ MJ/m³. The values of G_c and ℓ are listed in Table 2.

The cumulative fatigue variable is updated by the instantaneous crack-driving force. This force includes the positive elastic strain energy and accumulated stored plastic work:

$$x = \psi_e^+ + \psi_{p,hard} \tag{20}$$

$$D(t) = \int_0^t Heav(x\dot{x})|\dot{x}|dt \tag{21}$$

The Heaviside function in Eq. (21) selects positive increments of the crack-driving force. Thus, the fatigue variable D increases monotonically with cyclic loading. The accumulated stored plastic work acts as a local crack-driving force and also updates the fatigue history variable.

3.4 Three-layer numerical implementation using a residual-controlled staggered algorithm

The displacement equilibrium equation and phase-field evolution equation follow from variations of the displacement field u and phase field ϕ according to the Griffith energy-minimization principle.Displacement equilibrium equation and phase-field evolution

https://doi.org/10.5194/ms-2026-192
Preprint. Discussion started: 3 November 2026
© Author(s) 2026. CC BY 4.0 License.



mechanical sciences DISCUSSIONS

equation:

$$\begin{aligned} &\nabla\cdot\left[g(\phi)\tilde{\sigma}^{+}+\tilde{\sigma}^{-}\right]+b=0, && in\Omega \\ &\left[g(\phi)\tilde{\sigma}^{+}+\tilde{\sigma}^{-}\right]\cdot n=\bar{t} && ,on\partial\Omega_{f} \\ &u=\bar{u} && ,on\partial\Omega_{\mathrm{u}} \end{aligned} \tag{22}$$

$$\begin{aligned} &g'(\phi)\left[H_{n}^{k}+\psi_{p,hard}\right]+F(D)\frac{G_C}{\ell}\left(\varphi-\ell^{2}\Delta\phi\right)=0, && in\Omega \\ &\nabla\phi\cdot n=0 && ,on\partial\Omega \end{aligned} \tag{23}$$

The displacement and phase fields are solved with a residual-controlled staggered algorithm (Seleš et al., 2019). Each iteration updates the phase field, the crystal-plasticity mechanical field, and the virtual phase-field residual in sequence. Residual feedback then determines whether the current increment has converged.

Algorithm 1. Main steps of the residual-controlled staggered algorithm.

Algorithm: Residual-controlled incremental-iterative solution procedure

Input: Specify the convergence tolerance and import the converged state $\{u_n,\phi_n,H_n,D_n\}$.

1 Initialize increment $n+1$, set $k=0$, and inherit the state from increment n.

2 Layer-I UEL reads the latest stored H_{n+1}^{k} and D_{n+1}^{k}, solves the phase-field subproblem, and updates ϕ_{n+1}^{k}.

3 UMAT reads ϕ_{n+1}^{k} and updates the stress, crystal slip, hardening variables, and consistent tangent during the global mechanical equilibrium solution.

4 Layer-III UEL receives ψ_{e}^{+} and $\psi_{p,hard}$, updates H_{n+1}^{k} and D_{n+1}^{k}, and evaluates the residual $R_{dummy}^{\phi,k}$.

5 Calculate r_{u}^{k} and r_{ϕ}^{k} using Eq. (24), and evaluate r_{total}^{k} using Eq. (25).

6 If $r_{total}^{k}\le tol$, accept the current increment; otherwise, set k←k+1 and return to Step 2.

Output: Obtain the converged fields u_{n+1} and ϕ_{n+1}, together with the updated integration-point state variables.

The displacement residual and virtual phase-field residual are normalized separately. The dimensionless residuals at staggered iteration k are

$$r_{u}^{k}=\frac{\left\|R_{u}^{k}\right\|_{2}}{\max\left(\left\|F_{ext}\right\|_{2},F_{0}\right)};r_{\phi}^{k}=\frac{\left\|R_{dummy}^{\phi,k}\right\|_{2}}{\max\left(\left\|R_{dummy}^{\phi,0}\right\|_{2},R_{\phi,0}\right)} \tag{24}$$

where F_0 and $R_{\phi,0}$ are the reference values of the corresponding residuals. The total residual is the larger of the two values:

$$r_{total}^{k}=\max\left(r_{u}^{k},r_{\phi}^{k}\right) \tag{25}$$

$$r_{total}^{k}\le tol \tag{26}$$

The current load increment is accepted when Eq. (26) is satisfied. Otherwise, the staggered

https://doi.org/10.5194/ms-2026-192
Preprint. Discussion started: 3 November 2026
© Author(s) 2026. CC BY 4.0 License.



mechanical sciences DISCUSSIONS

iteration continues.

A three-layer overlapping UEL–UMAT–UEL element system is constructed in Abaqus. The first UEL layer solves the phase field. Standard mechanical elements in the second layer use the UMAT to update crystal slip, hardening variables, stress, and the material Jacobian. The third UEL layer recalculates the phase-field residual and returns the convergence state. All three discretizations use the same nodal topology and integration-point arrangement. Element-number mapping and common data blocks transfer ϕ, ψ_e^+, $\psi_{p,hard}$, H, D, and R_{dummy}^{ϕ}.

After the current increment satisfies Eq. (26), the state variables are committed and the solution proceeds to the next increment. Fig. 6 shows the calling sequence of the three user subroutines and the transfer of integration-point variables.

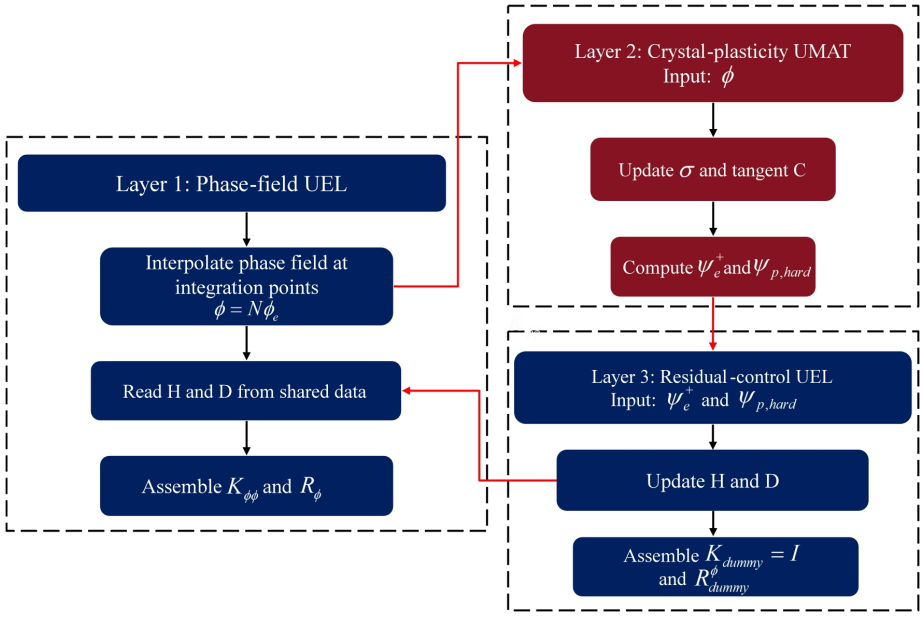


Fig. 6. Calling sequence and integration-point data transfer in the three-layer UEL–UMAT–UEL system.

4. Results and discussion

4.1 Material parameters and loading conditions

The grain-scale model uses a two-dimensional plane-strain discretization. The bearing-steel matrix in both models calls the three-layer UEL–UMAT–UEL system described in Section 3.4. The Al_2O_3 inclusion is linear elastic and does not undergo crystal slip or phase-field evolution. Table 2 lists the material parameters.

https://doi.org/10.5194/ms-2026-192
Preprint. Discussion started: 3 November 2026
© Author(s) 2026. CC BY 4.0 License.



mechanical sciences
DISCUSSIONS

Table 2. Parameters of the crystal plasticity–phase-field model and inclusion (Zhang et al., 2024; Lucarini et al., 2023; Zhang et al., 2025).

Parameter	Symbol	Matrix (bearing steel)	Inclusion (Al_2O_3)
Young's modulus	E	210 GPa	380 GPa
Poisson's ratio	ν	0.30	0.25
Initial critical resolved shear stress	$\tau_{c,0}$	350 MPa	—
Saturation critical resolved shear stress	$\tau_{c,s}$	480 MPa	—
Initial hardening modulus	h_0	2000 MPa	—
Reference shear rate	$\dot{\gamma}_0$	1.0×10^{-3} s^{-1}	—
Rate-sensitivity exponent	m	0.05	—
Fracture toughness	G_c	2.7 kN/m	—
Length-scale parameter	ℓ	5 μm	—
Stored-plastic-work fraction	η_h	0.05	—

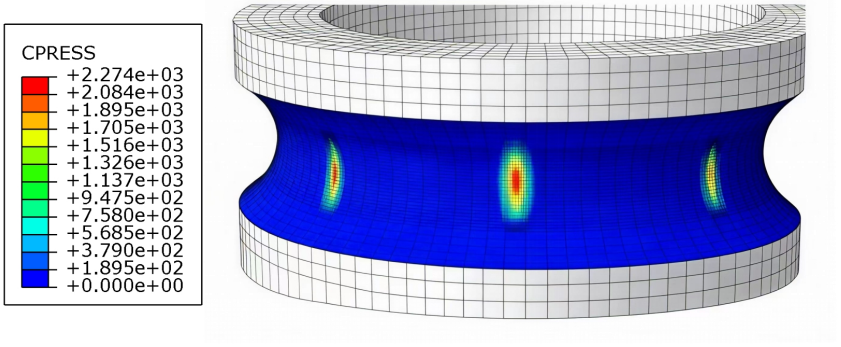


Fig. 7. Contact-pressure distribution on the inner-ring raceway.

The macroscale contact field of the inner-ring raceway is first analyzed under the reference condition to define the moving load of the grain-scale model. Fig. 7 shows a local elliptical contact patch in the loaded zone. The peak contact pressure is approximately 2.27 GPa. The platform selects the contact patch containing the pressure peak. It extracts the pressure distribution along the main section through the pressure center in the rolling direction. This gives the peak pressure p_0 and contact half-width a. These parameters define a two-dimensional moving Hertzian load on the top boundary of the grain-scale model. Let $x_c(t)$ denote the pressure center. The normal pressure p and tangential traction magnitude q on the top boundary are

https://doi.org/10.5194/ms-2026-192
Preprint. Discussion started: 3 November 2026
© Author(s) 2026. CC BY 4.0 License.



mechanical sciences DISCUSSIONS

$$p(x,t)=\begin{cases} p_0\sqrt{1-\left(\dfrac{x-x_c(t)}{\mathrm{a}}\right)^2} & ,\left|x-x_c(t)\right|\le a \\ 0 & ,\left|x-x_c(t)\right|>a \end{cases} \tag{27}$$

$$q(x,t)=\mu p(x,t)$$

The tangential traction acts opposite to the local relative sliding velocity. Under the same reference condition, the macroscale module automatically extracts and transfers p_0 = 2.27 GPa and a = 0.10 mm to the grain-scale module. The friction coefficient is μ = 0.05. Other parameter sets in the structural scans use their own p_0 and a values from the macroscale analyses.

One numerical cycle is defined as the movement of the pressure center from one side of the local polycrystalline model to the other. A fixed cycle-jump factor of J = 1000 is used. Within each numerical cycle, the crystal plasticity mechanical field and phase field are solved over the complete moving-load path. At the end of the cycle, the fatigue-history increment is multiplied by J and written into the next cycle. The equivalent cycle count is updated at the same time:

$$N_{eq}=JN_{num};\Delta D_{eq}=J\Delta D_{num} \tag{28}$$

where N_{num} and N_{eq} are the completed numerical-cycle count and the corresponding equivalent-cycle count. The quantities ΔD_{num} and ΔD_{eq} are the fatigue-history increments for one numerical cycle and after cycle jumping, respectively. When the maximum phase-field variable first satisfies $max(\phi)\ge 0.95$, the corresponding N_{eq} is recorded as the predicted RCF life.

4.2 RCF damage evolution with and without an inclusion

At the beginning of loading in the inclusion-free model, stored plastic work localizes below the surface in regions with high MOSS and favorable crystal orientations. Repeated passage of the moving load extends and connects the damage band along the rolling direction. The band then turns toward the free surface and forms a shallow and wide spall. Fig. 8 shows the phase-field evolution at different equivalent cycle counts. According to the $max(\phi)\ge 0.95$ criterion, the first saved failure frame that reaches the threshold corresponds to $N_{f,0}\approx 3.2\times 10^6$ cycles. Later frames show further crack growth and the evolution of the spall geometry.

The early high-ϕ region does not appear directly at the free surface. It largely coincides

https://doi.org/10.5194/ms-2026-192
Preprint. Discussion started: 3 November 2026
© Author(s) 2026. CC BY 4.0 License.



mechanical sciences
DISCUSSIONS

with the subsurface high-shear region. The damage first grows approximately parallel to the surface. It then reaches the surface under the local energy gradient. This sequence differs from rapid crack growth from a pre-existing notch in an ideal brittle material. It shows that accumulated stored plastic work contributes to crack initiation. Because the grain orientations are random, the boundary of the damage band does not exactly follow a contact-stress contour. Instead, several local high-value regions in neighboring grains connect and form an irregular boundary.

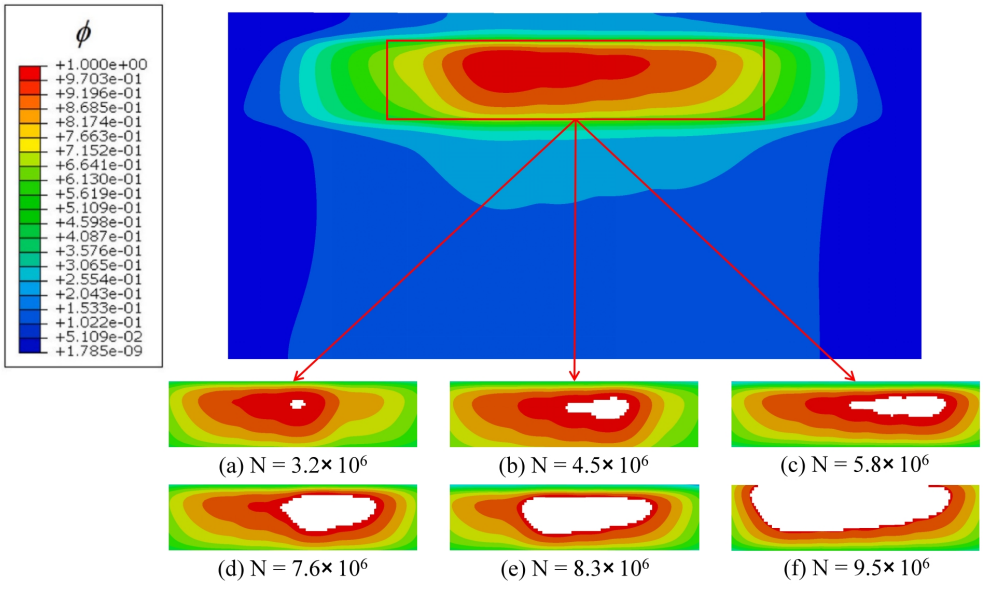


Fig. 8. Phase-field evolution and spall formation in the inclusion-free model at different equivalent cycle counts.

The inclusion-containing model has an elliptical Al_2O_3 inclusion at a depth of 50 μm. Its major and minor axes are 20 and 10 μm, respectively, and the major axis is parallel to the rolling direction. The inclusion is perfectly bonded to the matrix and is treated as a linear elastic material. The stiffness mismatch between Al_2O_3 and bearing steel causes strong concentrations of stress and plastic work near the ends of the ellipse. Fig. 9 shows the phase-field evolution. Phase-field damage first appears in the adjacent matrix. It then develops into asymmetric inclined damage bands along two main directions. The material mismatch and local cyclic plasticity caused by the inclusion therefore change the crack initiation site and growth path.

https://doi.org/10.5194/ms-2026-192
Preprint. Discussion started: 3 November 2026
© Author(s) 2026. CC BY 4.0 License.



mechanical sciences
DISCUSSIONS

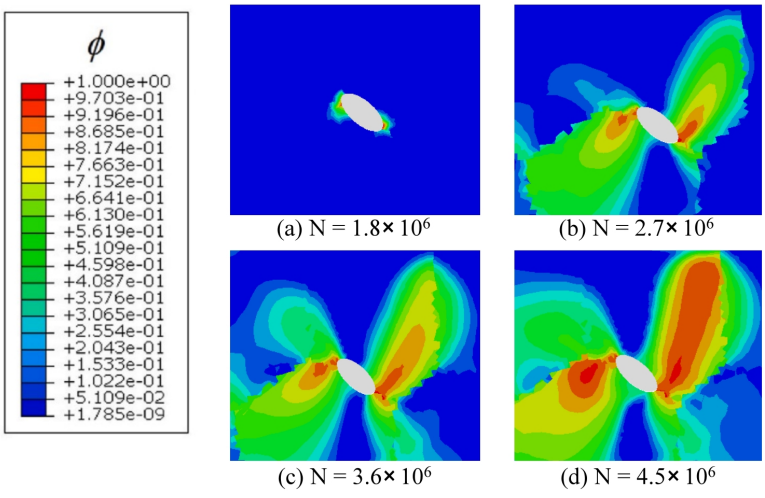


Fig. 9. Phase-field evolution in the model with an elliptical Al_2O_3 inclusion.

The first saved failure frame in the inclusion-containing model corresponds to $N_{f,inc} \approx 1.8\times10^{6}$ cycles. This life is approximately 43.8% lower than the 3.2 × 10^6 cycles of the inclusion-free model. The inclusion therefore accelerates RCF crack initiation and spall formation.

The spatial distribution of the driving force explains the life difference. Without an inclusion, plastic work develops over a relatively broad region. A continuous damage path forms only after several grains with favorable orientations become connected. With an inclusion, the stiffness discontinuity concentrates the driving force near the two ends of the ellipse. A continuous damage path forms earlier. Cracks therefore initiate and grow first in the matrix near the inclusion.

The predicted spall paths are compared with typical RCF morphologies reported for bearing steels. Fig. 10 shows numerical and experimental results for surface- and subsurface-initiated pitting (Glodež et al., 2007). Fig. 11 shows a butterfly structure around a subsurface inclusion (Evans, 2012) and a subsurface white-etching area (Evans et al., 2014). In the inclusion-free model, damage grows below the surface and then breaks through the surface. In the inclusion-containing model, inclined damage develops near the inclusion. These features agree with reported inclusion-induced RCF damage characteristics (Xiong et al., 2024; Cerullo, 2014).

https://doi.org/10.5194/ms-2026-192
Preprint. Discussion started: 3 November 2026
© Author(s) 2026. CC BY 4.0 License.

mechanical sciences
DISCUSSIONS

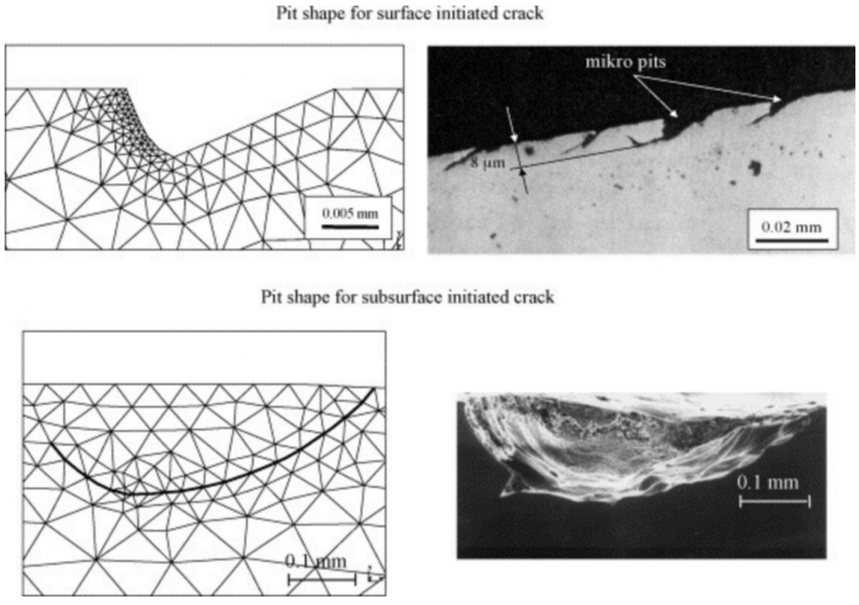


Fig. 10. Numerical and experimental morphologies of surface- and subsurface-initiated pitting (Glodež et al., 2007).

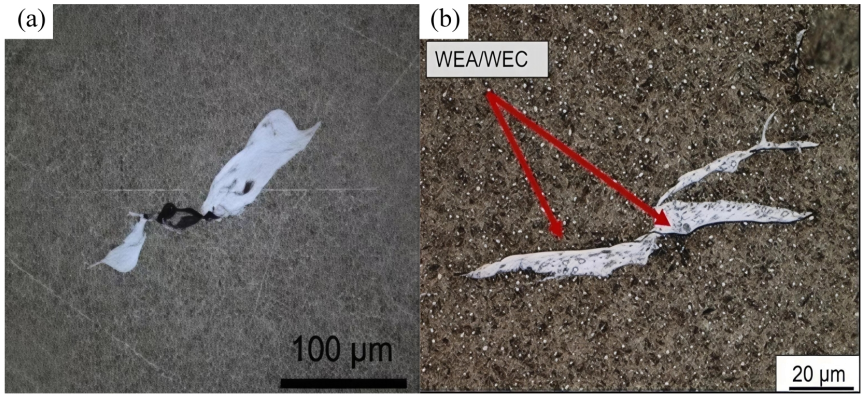


Fig. 11. (a) Butterfly structure around a subsurface inclusion (Evans, 2012); (b) subsurface white-etching area under rolling contact (Evans et al., 2014).

4.3 Effects of structural parameters on MOSS and RCF life

Before the parameter sweeps, we must verify Eq. (1). The reference life N_{ref} are 3.2×10^6 and 3.4×10^6 cycles for the inner and outer raceways, respectively. This value comes from the inclusion-free model in Section 4.2. This reference life is evaluated under D_w = 7.8 mm, f = 0.514, G_r = 5 µm, and n = 5000 r/min. Full crystal plasticity-phase-field simulations are too expensive for every design. Therefore, macro-scale MOSS is used as a proxy variable. Fig. 12 validates this mapping. It uses the rolling-element diameter D_w as a representative case. Fig.

https://doi.org/10.5194/ms-2026-192
Preprint. Discussion started: 3 November 2026
© Author(s) 2026. CC BY 4.0 License.



mechanical sciences DISCUSSIONS

12(a) shows the MOSS from the macro-scale contact analysis. Fig. 12(b) shows the phase-field life from the micro-scale model. The black points are the micro-scale simulation results. The solid curves are the predictions from Eq. (1). Both MOSS and phase-field life follow a strong power-law relation, despite the unavoidable scatter caused by random grain orientations. The slopes are -3.05 for the inner raceway and -2.90 for the outer raceway. We also verified the mapping for f and G_r using the identical procedure (results not shown for brevity). The same power-law mapping remains valid for all three parameters. Therefore, Eq. (1) is reliable for the subsequent parameter scans.

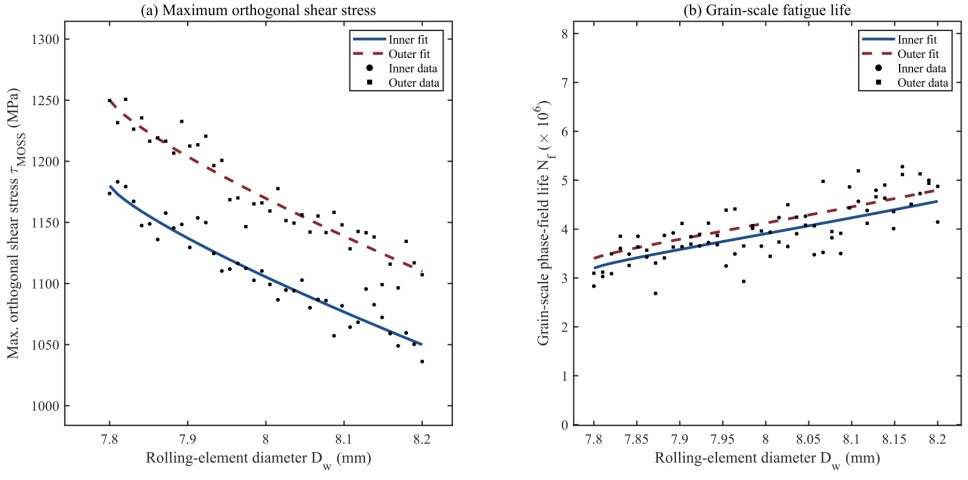


Fig. 12. Validation of the mapping relation between macro-scale MOSS and micro-scale phase-field fatigue life.

Regular parameter scans are performed for D_w = 7.80–8.20 mm with a step of 0.02 mm. The range of f is 0.514–0.528 with a step of 0.001. The range of G_r is 5–20 μm with a step of 1 μm. The speed n ranges from 5 to 20 × 10^3 r/min with a step of 1 × 10^3 r/min. The three scan tasks contain 336, 240, and 256 parameter sets, respectively. Each set undergoes a macroscale contact analysis. The inner- and outer-raceway MOSS values are extracted. Life is calculated with the power-law mapping based on the phase-field reference life in Section 2.4. The competing-failure equation then gives the overall bearing life.

In Figs. 13–15, panel (a) presents the inner-raceway MOSS response at two representative speeds. Panels (b) and (c) show the predicted inner- and outer-raceway lives, respectively. Panel (d) shows the overall bearing life from the competing-failure relation.

https://doi.org/10.5194/ms-2026-192
Preprint. Discussion started: 3 November 2026
© Author(s) 2026. CC BY 4.0 License.



mechanical sciences
DISCUSSIONS

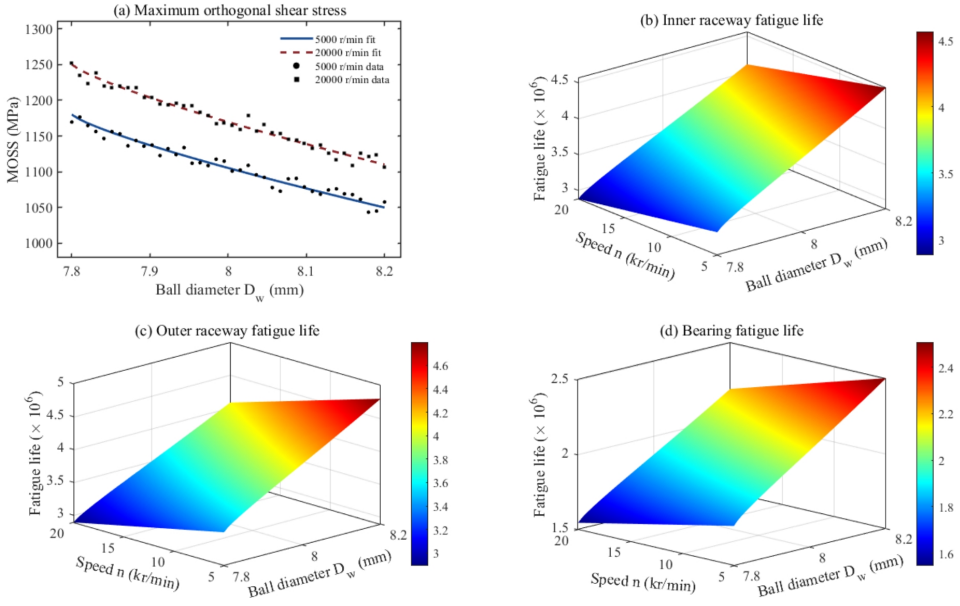


Fig. 13. Effects of rolling-element diameter and rotational speed on MOSS and predicted RCF life.

Within the examined speed range, increasing D_w from 7.80 to 8.20 mm increases the equivalent radius of curvature of the rolling element. The combined contact curvature decreases and the contact area expands. At 5,000 r/min, the MOSS decreases from approximately 1180 to 1050 MPa. At 20,000 r/min, it decreases from approximately 1250 to 1110 MPa. The predicted lives of both raceways increase. At higher speeds, inertial effects change the load distribution and cause a moderate overall life reduction. Subject to cage-pocket, minimum-wall-thickness, and assembly-space constraints, increasing D_w is an effective way to improve RCF life.

https://doi.org/10.5194/ms-2026-192
Preprint. Discussion started: 3 November 2026
© Author(s) 2026. CC BY 4.0 License.



mechanical sciences
DISCUSSIONS

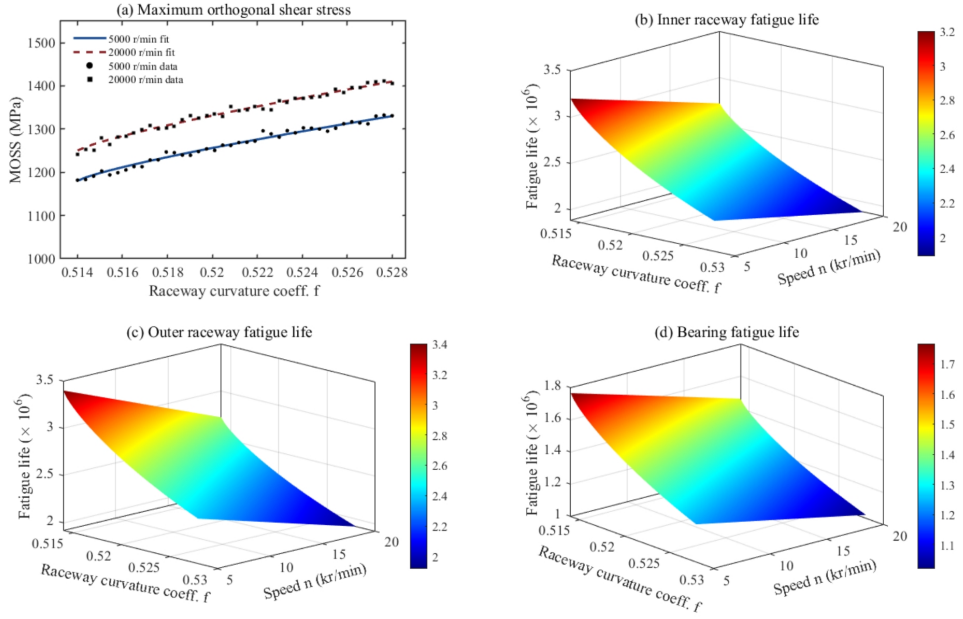


Fig. 14. Effects of raceway curvature coefficient and rotational speed on MOSS and predicted RCF life.

At each speed, increasing the curvature coefficient from 0.514 to 0.528 reduces the conformity between the raceway and rolling element. The MOSS increases. At 5000 r/min, the MOSS increases from 1180 to 1330 MPa. At 20000 r/min, it increases from 1250 to 1410 MPa. The inner-raceway, outer-raceway, and overall bearing lives decrease rapidly. Compared with the parameter ranges of D_w and G_r, f produces a larger change in MOSS. Raceway curvature therefore causes the largest life variation in the present parameter ranges. Reducing f can lower the MOSS and improve RCF life. It is the primary geometric variable for life-oriented parameter adjustment.

https://doi.org/10.5194/ms-2026-192
Preprint. Discussion started: 3 November 2026
© Author(s) 2026. CC BY 4.0 License.



mechanical sciences
DISCUSSIONS

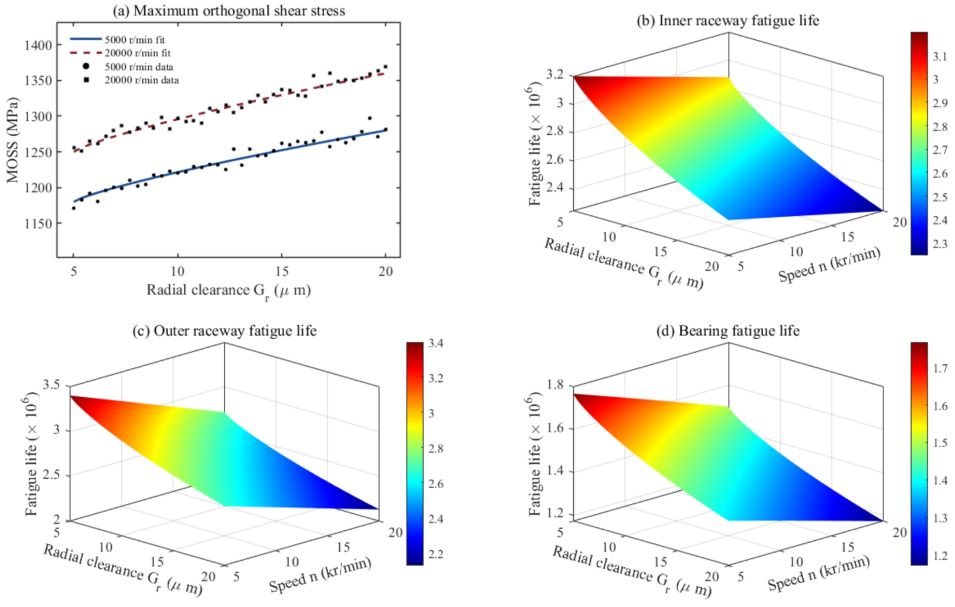


Fig. 15. Effects of radial clearance and rotational speed on MOSS and predicted RCF life.

At each speed, increasing the positive radial clearance from 5 to 20 μm reduces the number of loaded rolling elements and makes the load distribution less uniform. The local load on the most heavily loaded rolling element increases. At 5,000 r/min, the MOSS increases from approximately 1180 to 1280 MPa. At 20,000 r/min, it increases from approximately 1250 to 1360 MPa. The predicted life decreases accordingly. Within the present parameter range, a smaller positive clearance improves the load distribution and extends RCF life. It is therefore a preferred variable in the platform's parameter-feedback process.

5. Conclusions

In this study, an integrated multiscale rolling contact fatigue (RCF) analysis platform is proposed for rolling bearings. This platform automatically performs parametric modeling, macroscale contact analysis, and grain-scale damage calculation. It significantly improves analysis efficiency. It also reduces manual operations and simulation time. A coupled crystal plasticity-phase-field model is used. This model accurately captures damage evolution under rolling contact.

Simulation results show the effects of nonmetallic inclusions. These inclusions concentrate local stress. They also accumulate stored plastic work. They lead to earlier crack initiation. Therefore, they significantly reduce the predicted fatigue life. For structural parameters, increasing the rolling-element diameter reduces the maximum orthogonal shear

https://doi.org/10.5194/ms-2026-192
Preprint. Discussion started: 3 November 2026
© Author(s) 2026. CC BY 4.0 License.



mechanical sciences
DISCUSSIONS

stress (MOSS). It extends the fatigue life. Increasing the raceway curvature coefficient or the positive radial clearance increases the maximum orthogonal shear stress. It shortens the fatigue life. These findings provide a direct theoretical basis for the life-oriented adjustment of key bearing parameters.

Acknowledgements

This work was sponsored by National Natural Science Foundation of China (Grant No. 52505154 and 12432006);

References

[1] Harris T A, Kotzalas M N. Rolling Bearing Analysis: Essential Concepts of Bearing Technology. 5th ed. CRC Press, 2006.

[2] Lundberg G, Palmgren A. Dynamic capacity of rolling bearings. Acta Polytechnica, Mechanical Engineering Series, 1947, 1(3): 1–52. https://doi.org/10.1115/1.4009930

[3] Ioannides E, Harris T A. A new fatigue life model for rolling bearings. Journal of Tribology, 1985, 107(3): 367–378. https://doi.org/10.1115/1.3261081

[4] Jones A B. Ball motion and sliding friction in ball bearings. Journal of Basic Engineering, 1959, 81(1): 1–12. https://doi.org/10.1115/1.4009930

[5] de Mul J M, Vree J M, Maas D A. Equilibrium and associated load distribution in ball and roller bearings loaded in five degrees of freedom while neglecting friction. Journal of Tribology, 1989, 111(1): 142–148. https://doi.org/10.1115/1.3261864

[6] Kang Y, Shen P, Huang C, et al. A modification of the Jones–Harris method for deep-groove ball bearings. Tribology International, 2006, 39(11): 1413–1420. https://doi.org/10.1016/j.triboint.2005.12.005

[7] Fang B, Zhang J, Yan K, et al. A comprehensive study on the speed-varying stiffness of ball bearing under different load conditions. Mechanism and Machine Theory, 2019, 136: 1–13. https://doi.org/10.1016/j.mechmachtheory.2019.02.012

[8] Cheng H C, Zhang Y M. Effect of spatial position of the ball and random parameters on rolling bearing fatigue life. Journal of the Brazilian Society of Mechanical Sciences and Engineering, 2022, 44: 246. https://doi.org/10.1007/s40430-022-03551-6

[9] Hill R, Rice J R. Constitutive analysis of elastic-plastic crystals at arbitrary strain. Journal of the Mechanics and Physics of Solids, 1972, 20(6): 401–413. https://doi.org/10.1016/0022-5096(72)90017-8

[10] Huang Y. A user-material subroutine incorporating single crystal plasticity in the ABAQUS finite element program. Cambridge, MA: Harvard University, Division of Applied Sciences, Report MECH-178, 1991.

[11] McDowell D L, Dunne F P E. Microstructure-sensitive computational modeling of fatigue crack formation. International Journal of Fatigue, 2010, 32(9): 1521–1542. https://doi.org/10.1016/j.ijfatigue.2010.01.003

[12] Wan V V C, MacLachlan D W, Dunne F P E. A stored energy criterion for fatigue crack nucleation in polycrystals. International Journal of Fatigue, 2014, 68: 90–102. https://doi.org/10.1016/j.ijfatigue.2014.06.001

[13] Zhang Z, Shen F, Ke L L. A dislocation density-based crystal plasticity damage model for rolling contact fatigue of gradient grained structures. International Journal of Fatigue, 2024, 179: 108038. https://doi.org/10.1016/j.ijfatigue.2023.108038

[14] Xiong G, Dong Q, Shi X, et al. An elastic-plastic damage model of rolling contact fatigue considering

https://doi.org/10.5194/ms-2026-192
Preprint. Discussion started: 3 November 2026
© Author(s) 2026. CC BY 4.0 License.



mechanical sciences
DISCUSSIONS

nonmetallic inclusion. International Journal of Fatigue, 2024, 188: 108511.
https://doi.org/10.1016/j.ijfatigue.2024.108511
[15] Vijay A, Sadeghi F. A crystal plasticity and cohesive element model for rolling contact fatigue of bearing steels. Tribology International, 2022, 173: 107607. https://doi.org/10.1016/j.triboint.2022.107607
[16] Han X, Li S, Sun C, et al. Modelling micropit formation in rolling contact fatigue of bearings with a crystal plasticity damage theory coupled with cohesive finite elements. Engineering Fracture Mechanics, 2024, 297: 109873. https://doi.org/10.1016/j.engfracmech.2024.109873
[17] Francfort G A, Marigo J J. Revisiting brittle fracture as an energy minimization problem. Journal of the Mechanics and Physics of Solids, 1998, 46(8): 1319–1342. https://doi.org/10.1016/S0022-5096(98)00034-9
[18] Miehe C, Welschinger F, Hofacker M. Thermodynamically consistent phase-field models of fracture: Variational principles and multi-field FE implementations. International Journal for Numerical Methods in Engineering, 2010, 83(10): 1273–1311. https://doi.org/10.1002/nme.2861
[19] Ambati M, Gerasimov T, De Lorenzis L. A review on phase-field models of brittle fracture and a new fast hybrid formulation. Computational Mechanics, 2015, 55(2): 383–405. https://doi.org/10.1007/s00466-014-1109-y
[20] Golahmar A, Niordson C F, Martínez-Pañeda E. A phase field model for high-cycle fatigue: Total-life analysis. International Journal of Fatigue, 2023, 170: 107558. https://doi.org/10.1016/j.ijfatigue.2023.107558
[21] Polančec T, Lesičar T, Tonković Z, et al. Modelling of rolling-contact fatigue pitting phenomena by phase field method. Wear, 2023, 532–533: 205068. https://doi.org/10.1016/j.wear.2023.205068
[22] Lucarini S, Dunne F P E, Martínez-Pañeda E. An FFT-based crystal plasticity phase-field model for micromechanical fatigue cracking based on stored energy density. International Journal of Fatigue, 2023, 172: 107670. https://doi.org/10.1016/j.ijfatigue.2023.107670
[23] Zhang Z, Huang G Y, Shen F, et al. A phase field model for spalling failure due to rolling contact fatigue. International Journal of Fatigue, 2025, 198: 109006. https://doi.org/10.1016/j.ijfatigue.2025.109006
[24] Khan M T H, Rezwana S. A review of CAD to CAE integration with a hierarchical data format (HDF)-based solution. Journal of King Saud University–Engineering Sciences, 2021, 33(4): 248–258.
https://doi.org/10.1016/j.jksues.2020.04.009
[25] Li C, Wei P, Luo X, et al. An unified CAD/CAE/VR tool for ship structure design and evaluation based on multi-domain feature mapping. Ocean Engineering, 2023, 280: 114888.
https://doi.org/10.1016/j.oceaneng.2023.114888
[26] Seleš K, Lesičar T, Tonković Z, et al. A residual control staggered solution scheme for the phase-field modeling of brittle fracture. Engineering Fracture Mechanics, 2019, 205: 370–386.
https://doi.org/10.1016/j.engfracmech.2018.09.027
[27] Glodež S, Fajdiga G, Kramar J. Pitting formation due to surface and subsurface initiated fatigue crack growth in contacting mechanical elements. Wear, 2007, 262(9–10): 1217–1224.
https://doi.org/10.1016/j.wear.2006.11.016
[28] Evans M H. White structure flaking (WSF) in wind turbine gearbox bearings: effects of “butterflies” and white etching cracks (WECs). Materials Science and Technology, 2012, 28(1): 3–22.
https://doi.org/10.1179/026708311X13135950699254
[29] Evans M H, Wang L, Wood R J K. Formation mechanisms of white etching cracks and white etching area under rolling contact fatigue. Proceedings of the Institution of Mechanical Engineers, Part J: Journal of

https://doi.org/10.5194/ms-2026-192
Preprint. Discussion started: 3 November 2026
© Author(s) 2026. CC BY 4.0 License.



mechanical sciences
DISCUSSIONS

1 Engineering Tribology, 2014, 228(10): 1047–1062. https://doi.org/10.1177/1350650114525363
2 [30] Cerullo M. Sub-surface fatigue crack growth at alumina inclusions in AISI 52100 roller bearings. Procedia
3 Engineering, 2014, 74: 333–338. https://doi.org/10.1016/j.proeng.2014.06.274